scientific reports

OPEN

snRNA-seq reveals key transcription factors in the inflammatory response of microglia after intracerebral hemorrhage

Zhuojin Wu[1,3], Danyang Chen[2,3], Shiling Chen[2], Ge Zhang[2], Xuan Wu[2], Kai Shu[1], Chao Pan[2✉] & Zhouping Tang[2✉]

Intracerebral hemorrhage (ICH) is a severe neurological disease with limited treatment options. Microglia, the primary immune cells of the brain, contribute significantly to secondary injury following ICH, exhibiting heterogeneity in response across different stages of ICH. However, the exact mechanisms regulating this process remain incompletely elucidated. In this study, we utilized single-nucleus RNA sequencing (snRNA-seq) in conjunction with the ICH model of mice to establish a comprehensive single-nucleus transcriptomic atlas for ICH and further elucidate its pathogenesis to identify potential therapeutic targets. We identified five principal brain clusters with cell-type specific gene expression patterns. Focused on microglia and inflammation-associated subgroup, we identified 8 distinct microglia subtypes and the key transcription factors (TFs) involved in the inflammatory response of microglia following ICH, including *Stat2*, *Stat1*, *Irf7*, *Nfkb1*, *Etv6*, *Cebpb*, *Batf*, and *Bach1*. Notably, *Stat2* and *Stat1* were identified as the most central TFs. In vitro experiments revealed that inhibiting *Stat2* and *Stat1* can attenuate the inflammatory response in microglia after ICH. Overall, our findings enhance the understanding of cell responses in ICH and highlight potential therapeutic targets, specifically suggesting that inhibiting STAT1 and STAT2 could mitigate microglial-mediated inflammation in ICH.

Keywords Intracerebral hemorrhage; single-nucleus RNA sequencing, Microglia, Inflammation, Transcription factor

Intracerebral hemorrhage (ICH) accounts for 10% – 15% of all stroke cases and is characterized by high incidence and mortality[1]. The pathophysiology involves primary injury from the hematoma and secondary injury driven by neuroinflammation and cell death[2,3]. As the brain's resident immune cells, microglia significantly contribute to secondary injury post-ICH. While exacerbate damage through the release of pro-inflammatory cytokines and reactive oxygen species, microglia are also essential for debris clearance and tissue repair. Crucially, emerging evidence indicates that microglia exhibit substantial functional and transcriptional heterogeneity across different stages of ICH[4]. However, the precise regulatory mechanisms governing this dynamic microglial response, particularly the specific molecular drivers of their detrimental inflammatory phenotype, remain incompletely understood, hindering the development of targeted anti-inflammatory therapies.

In recent years, single-cell RNA sequencing (scRNA-seq) has achieved breakthroughs in the field of ICH research, offering a new perspective for dissecting cellular heterogeneity and the spatiotemporal dynamics of pathological processes. Zhang et al. were the first to establish an scRNA-seq dataset of diverse immune cell populations in human perihematomal edema tissues, and found that the SPP1 signaling pathway acts as a key bridge for crosstalk between microglial subtypes during ICH progression[5]. Furthermore, Wang et al. constructed the first full-brain spatiotemporal atlas of a mouse ICH model by integrating spatial transcriptomics (Stereo-seq) with scRNA-seq and identified 17 ICH-associated cell subpopulations[6]. However, traditional whole-genome RNA sequencing and scRNA-seq are sensitive to tissue dissociation stress, which tends to result in the loss of fragile cell types (e.g., specific neuronal subpopulations) and may obscure transcriptional information at

[1]Department of Neurosurgery, Tongji Hospital, Tongji Medical College, Huazhong University of Science and Technology, Wuhan, China. [2]Department of Neurology, Tongji Hospital, Tongji Medical College, Huazhong University of Science and Technology, Wuhan 430030, China. [3]Zhuojin Wu MD and Danyang Chen MD contributed equally to this work. ✉email: punctualpc@163.com; ddjtzp@163.com

critical pathological stages. In comparison, single-nucleus RNA sequencing (snRNA-seq) can reduce cell bias and stress responses caused by tissue dissociation. Notably, snRNA-seq primarily captures nuclear transcripts, which underrepresent cytoplasmic mRNA species compared to scRNA-seq. However, this difference is offset by snRNA-seq's superior ability to preserve nuclear-enriched transcripts, such as those encoding transcription factors and chromatin regulators, which are critical for deciphering regulatory networks in pathological processes. It also shows high compatibility with frozen samples, thus serving as an effective alternative and complement to scRNA-seq. Huang et al. combined snRNA-seq and bulk RNA-seq to reveal the molecular mechanism of thalamus haemorrhage-induced central poststroke pain. However, the most common area for spontaneous ICH is the basal ganglia region.

Transcription factors (TFs) are pivotal regulators of the cellular function. Previous studies have indicated that several key TFs are involved in ICH pathogenesis: the neuroprotective nuclear factor-erythroid 2-related factor 2 (Nrf2) mitigates ICH-induced brain injury[7,8]; the pro-inflammatory tonicity-responsive enhancer-binding protein (TonEBP), which is upregulated in perihematomal microglia, exacerbates neuroinflammation by enhancing nuclear factor-κB (NF-κB) signaling via PELI[9]; and several other TFs are extensively implicated in ICH pathogenesis through the classic NF-κB and JAK/STAT pathways[10–12]. However, these discoveries failed to resolve the differential TF regulatory mechanisms within specific microglial subpopulations and the spatiotemporal dynamics of key pathways.

Accordingly, this study aims to employ snRNA-seq to build a comprehensive single-nucleus transcriptome map of ICH mice, systematically explore the heterogeneity of microglia at different post-ICH periods, and investigate the key transcription factors involved in the inflammatory response.
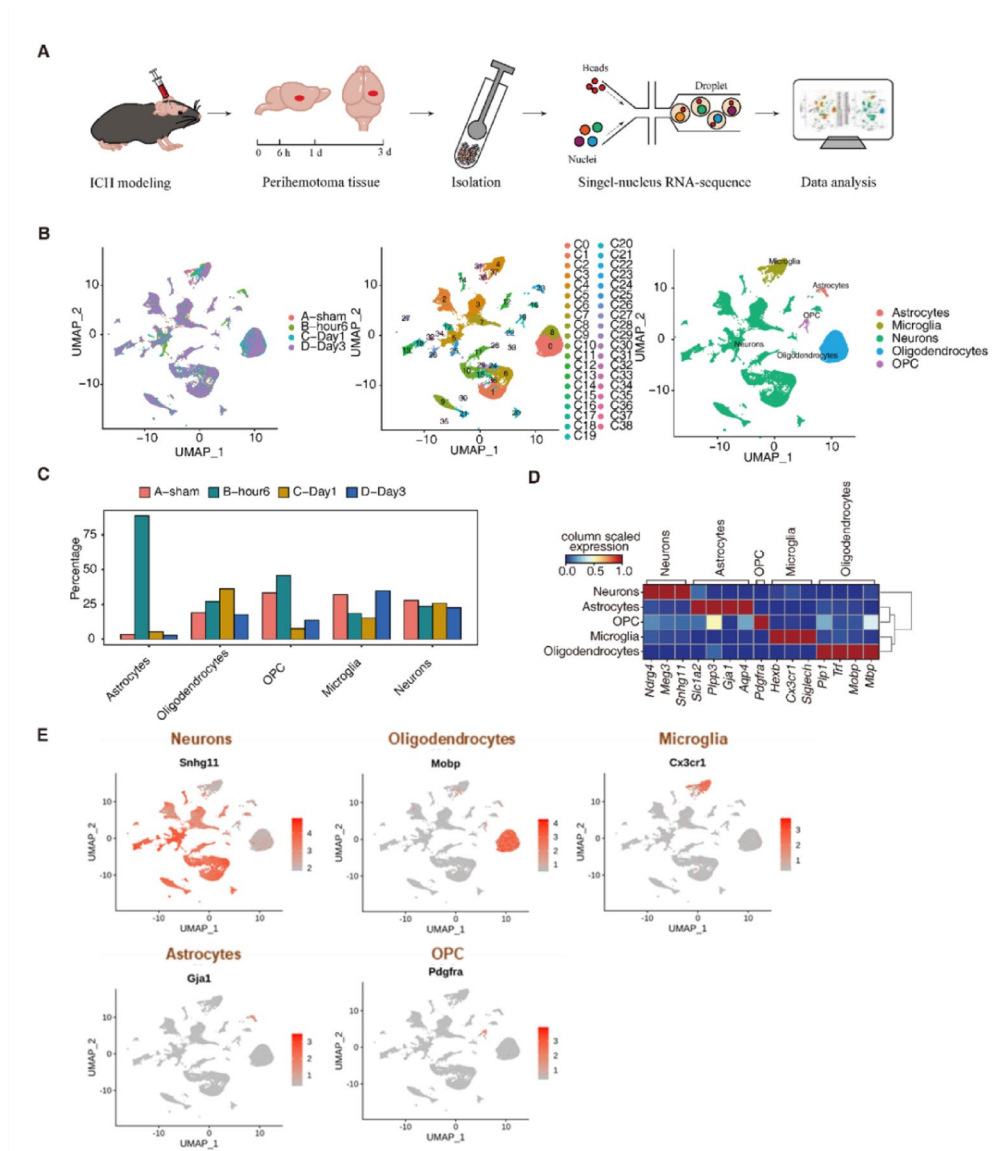
Result

Identification of major brain cell types and their overall changes after ICH

To explore the dynamic changes in cellular heterogeneity and differential gene expression following ICH, we utilized an autologous blood injection method to establish ICH mouse model. Perihematomal tissues were collected from ICH mice at the hyperacute phase (6 h), acute phase (24 h), and subacute phase (72 h), as well as from corresponding regions in the sham-operated group for snRNA-seq (Fig. 1A). After quality control, a total of 45,608 single-nucleus transcriptomes were obtained from the four samples. Unsupervised clustering analysis identified 39 distinct cell clusters (Fig. 1B). Using the sctype software and previously reported marker genes for brain cells, five major cell types were identified: Astrocytes (AC), Microglia (MG), Neurons(Neu), Oligodendrocytes (OL), and Oligodendrocyte Progenitor Cells (OPCs). Neurons were the most abundant cell type detected, followed by Oligodendrocytes and Microglia, with fewer Astrocytes and OPCs (Fig. 1B). And we validated the cell type in this study with previously published marker genes(Fig. 1D and E). Statistical analysis revealed that astrocytes were predominantly found in the hyperacute phase (B-hour6), OPCs had a higher proportion in the hyperacute phase but significantly decreased in the acute phase (C-Day1), and microglia were more prevalent in the subacute phase (D-Day3), while the proportion of neurons remained nearly constant across different stage (Fig. 1C, S1A). Functional enrichment analysis and pathway analysis revealed cell-type specific or shared biological and molecular function. Microglia are primarily enriched in the lysosomal pathway, participating in hematoma clearance and the regulation of neuroinflammation. Astrocytes are mainly enriched in the NOD-like receptor signaling pathway, involved in immune surveillance and inflammasome activation. Oligodendrocytes are predominantly enriched in lipid metabolic processes, contributing to the maintenance of myelin homeostasis. Oligodendrocyte precursor cells (OPCs) are mainly enriched in cell adhesion and differentiation, which facilitates lineage regeneration. Neurons are primarily enriched in redox reactions and nervous system development, potentially associated with antioxidant defense following ICH(Fig.S1B, S1C). These findings reflect the heterogeneity of cellular responses during different phases of ICH.

Unique gene expression characteristics of microglia subpopulations

As the resident immune cells in the brain, microglia are responsible for carrying out remarkable and multiple functions during ICH. In our study, we identified 3,183 microglia and eight unique cell clusters (MG0-MG7). MG0, MG3, and MG4 were predominantly derived from the sham and ICH-3d groups, while the MG2 accounted for 59.57% in the ICH-6 h group and 37.84% in the ICH-1d group (Fig. 2A and B). Cluster MG0 was characterized by high expression of homeostatic microglia marker genes(*Siglech*, *Cx3cr1*, *Tmem119*, *Hexb*), and functional enrichment analysis revealed associations with signal transduction, lysosome, and glycosphingolipid biosynthesis, indicating that MG0 represents homeostatic microglia[13–15]. Cluster MG1 exhibited lower specificity in gene expression but relatively higher levels of *Ccl12* and *Pla2g4*, suggesting that MG1 might be transitional or early-activated microglia[16,17]. Cluster MG2 showed high expression of chemokine genes(*Ccl3*, *Ccl4*) and proinflammatory cytokine genes (*Il12b*, *Il1b*, *Tnf*), and was directly enriched in the core inflammatory and immune response pathways (NF-κB, tumor necrosis factor (TNF), and Toll-like receptor signaling(TLR) pathways), indicating that MG2 is the primary cluster involved in inflammatory and immune responses[18,19]. Cluster MG3 demonstrated high expression of macrophage marker genes(*F13a1*, *Mrc1*, *Dab2*, *Ms4a7*), traditional M2 marker genes(*Arg1*, *Tgfbi*), and metabolism-related gene *Apoe*, with enrichment in cholesterol metabolism and intestinal immune network pathways[20,21]. Cluster MG4 was characterized by the high expression of cell proliferation-related genes (*Top2a*, *Knl1*, *Kif11*, *Mki67*), with enrichment in mitosis, cell cycle, and cell differentiation pathways, indicating that MG4 represents proliferating microglia[21]. Cluster MG5 showed high expression of *Apod* and oligodendrocyte marker genes(*Plp1*, *Trf*, and *Mobp*), and functional enriched in lipid metabolism, myelin formation and cell adhesion, which may play a significant role in oligodendrocyte heterogeneity, myelin maintenance, demyelination and remyelination[14,22]. Cluster MG6 and cluster MG7 were enriched in cell adhesion, neural development, synaptic transmission, and calcium signaling pathways, which may mainly participates in interactions with neurons (Fig. 2C, S2A, S2B).
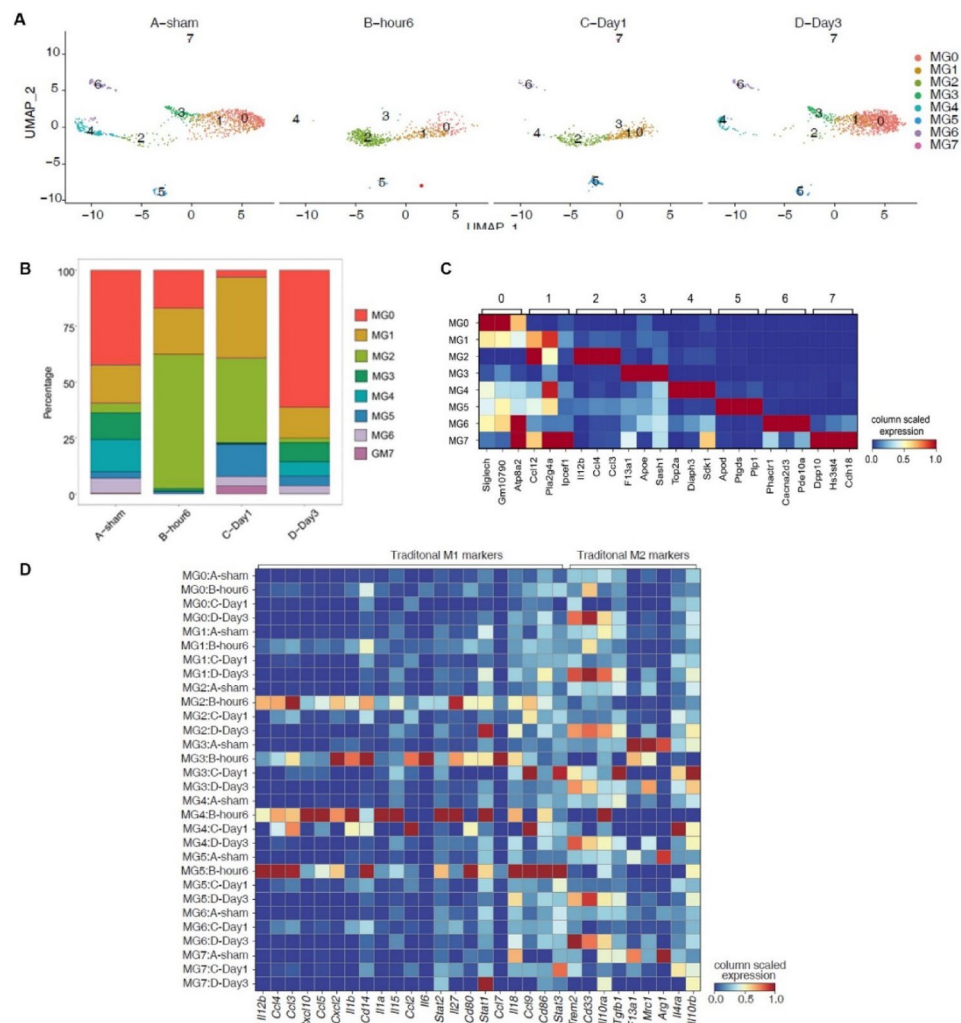
Fig. 1. Single nucleus RNA-seq analysis of brain tissue of mouse recapitulates transcriptome atlas in ICH. (**A**) Graphical diagram of single nucleus isolation and RNA-seq experimental setup. (**B**) UMAP plot of composite single-cell transcriptomic profiles from all 4 samples. Sample origin, cell clustering, and cell annotation results are shown from left to right. (**C**) Bar plot comparing the proportions of cell populations of each cell type within each sample group. (**D**) Unsupervised clustering heatmap showing the expression of representative genes annotated by cell types in each cell type. (**E**) UMAP showing the expression of selected marker genes. Oligodendrocyte Progenitor Cells (OPC).

Furthermore, heatmap revealed the temporal dynamic changes of M1/M2 marker genes in microglial cell subpopulations(Fig. 2D). M1 genes such as *Ccl3*, *Cxcl10*, *Il6*, and *Cd86* were predominantly upregulated at ICH-6 h, whereas M2-associated genes like *Tgfb1* and *Arg1* were most prominently expressed at ICH-3d. Notably, clusters MG2-5 demonstrated higher expression of M1 genes during the hyperacute phase, while M2 genes were relatively upregulated during the acute and subacute phases, suggesting a potential transition from M1 to M2 phenotypes in these microglial subtypes throughout the progression of ICH. Conversely, the MG1 cluster exhibited similar levels of M1 and M2 gene expression, while MG0, MG6, and MG7 consistently showed higher expression of M2-associated genes across different time points. Collectively, this section reveals the pronounced heterogeneity of microglial responses across different ICH phases.

Temporal diversification and functional reprogramming of microglia after ICH

To explore the differentiation trajectory of microglia following ICH, we used Monocle2 analysis and found five distinct microglial states (S1-S5) and two major differentiation pathways (Fig. 3A and B). S1 showed high expression of *Pchd9*, *Apod*, *Phactr1*, related to cell adhesion and neurodevelopment; S2 had elevated levels of metabolism-related gene(*APOE*, *SAA3*) and cell proliferation-related genes (*Top2a*); S3 specifically expressed
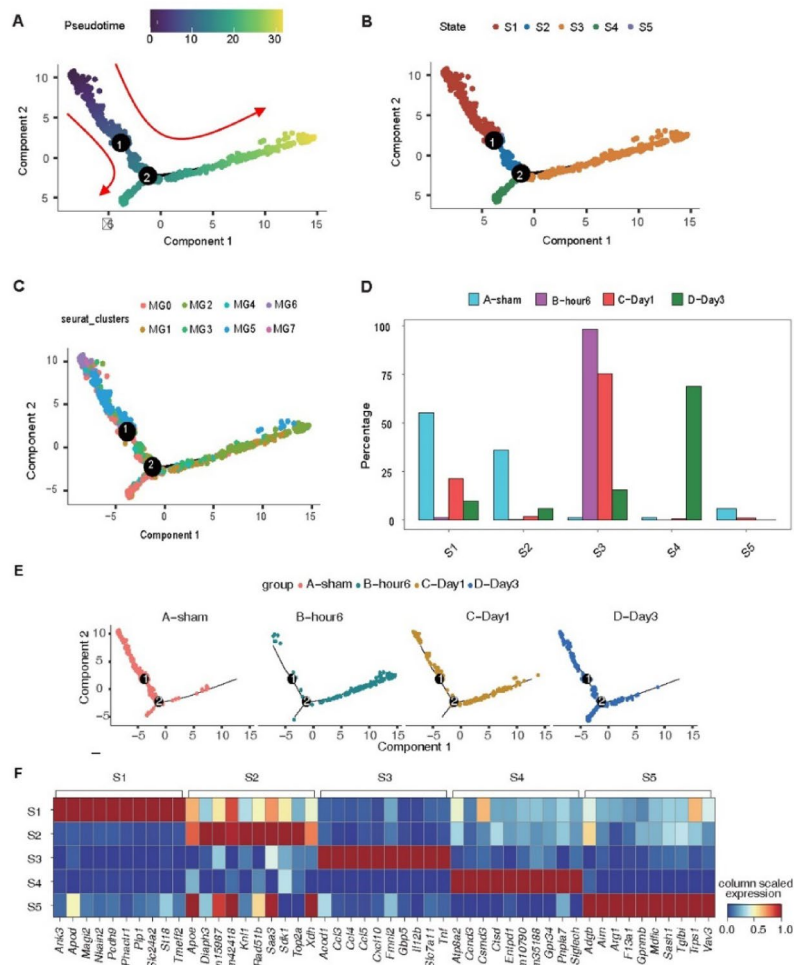
Fig. 2. Subpopulation analysis of microglia. (**A**) UMAP shows the regrouping of microglia; (**B**) The bar graph showing the proportion of different subsets of microglial cells in each sample. (**C**) Expression of Top 3 marker genes in each subgroup of microglia. (**D**) Unsupervised clustering heatmap showing relative expression (z score, row scaled) levels of M1 and M2 marker genes in microglia.

pro-inflammatory genes such as *Ccl3*, *Ccl4*, *Ccl5* and *Tnf*; S4 was characterized by signature genes involved in apoptosis and endocytosis (*Ccnd3*, *Entpd1* (CD39), *Siglech* (CD33), *Ctsd*); S5 was enriched in neuroprotective genes (*Arg1*, *F13a1*, *Tgfbi*). Over the post-ICH timeline, microglial state distribution evolved: primarily in homeostatic/proliferative states S1/S2 (sham), shifting acutely to inflammatory state S3 (ICH-6 h, ICH-1d), and progressing by ICH-3d to a broad distribution encompassing all states, with a significant presence in phagocytic/repair state S4. (Fig. 3C-F).

To identify dynamic gene expression patterns after ICH, we employed time course sequencing data analysis(TCseq) and 10 time-dependent gene clusters (Cluster 1–10) were revealed (Fig. 4A-C). Three clusters (Cluster 2, 8, 10) demonstrated significant associations with neuroinflammatory processes and microglial activation dynamics. Clusters 2 and 10 exhibited hyperacute upregulation followed by downregulation, with enrichment in inflammatory responses. Cluster 2, enriched in immune response, TNF production, NF-κB signaling, was implicated in initiating pro-inflammatory microglial activation (M1-like polarization). Cluster 10 was enriched in positive regulation of TNF and IL-4 production, suggesting a transient immunomodulatory response, potentially involving early anti-inflammatory/reparative (M2-like) microglial functions. Cluster 8 showed sustained expression during hyperacute and acute phases, enriched in inflammatory responses, translation, and gene expression regulation, indicating a role in maintaining microglial activity and facilitating functional adaptation. Conversely, Clusters 1, 3, and 9 were acutely upregulated, reflecting specialized microglial adaptations during tissue damage resolution: Cluster 1, enriched in lipid metabolism, ER stress, and protein folding, suggests involvement in lipid processing for membrane repair/efferocytosis and managing cellular stress. Cluster 3, characterized by enrichment in cell adhesion and migration, implicates enhanced microglial motility for targeted recruitment to lesion sites. Cluster 9, showing enrichment in chemical synaptic transmission and ion transport, may modulate neuron-microglia communication or synaptic environment remodeling.Clusters
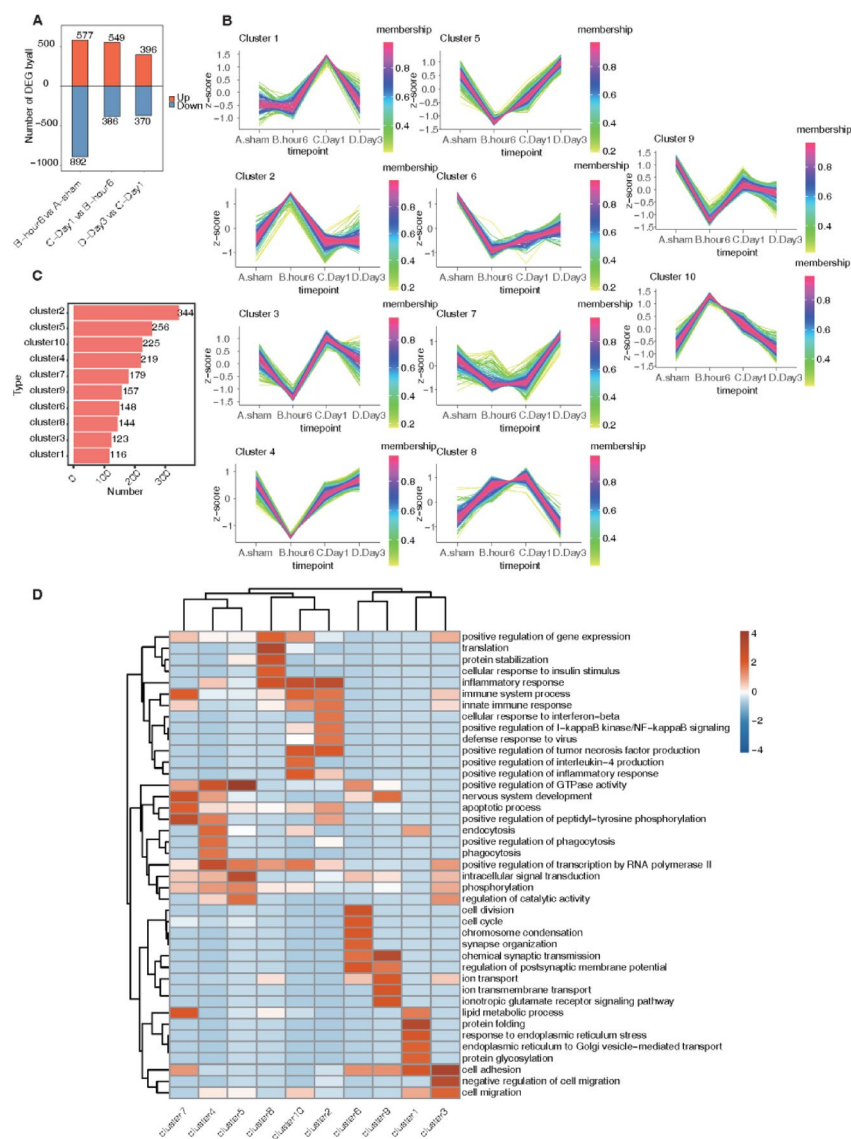
Fig. 3. Trajectory analysis of microglia. (**A**). Pseudotime analysis of microglia using Monocle, display based on state progression through pseudotime (**B**), Seurat-based clusters (**C**) and tissue origin (**E**). (**D**) The bar showing the proportion of microglia in each group in different states through pseudotime (**F**). Unsupervised clustering Heatmap showing relative expression (z score, row scale) levels of pseudotime state marker genes in microglia.

4–7 exhibited hyperacute downregulation followed by upregulation, indicating a shift towards reparative and homeostatic functions: Cluster 4, enriched for processes related to endocytosis and phagocytosis, directly supports phagocytic clearance (efferocytosis) of debris. Cluster 5, associated with GTPase activity, intracellular signaling, and phosphorylation, facilitates intracellular signaling required for functional responses. Cluster 6, enriched in cell cycle and differentiation, may relate to microglial proliferation or phenotypic modulation. Cluster 7, showing enrichment in lipid metabolism, apoptosis, and neurodevelopment, points to roles in lipid homeostasis, regulated cell death, and potential neurorestorative processes(Fig. 4B and D). Collectively, these temporally regulated clusters delineate the transition of microglia from initial hyperinflammatory states (Clusters 2,8,10) towards damage resolution, homeostasis restoration, and potential repair (Clusters 1,3,4–7,9) following ICH.
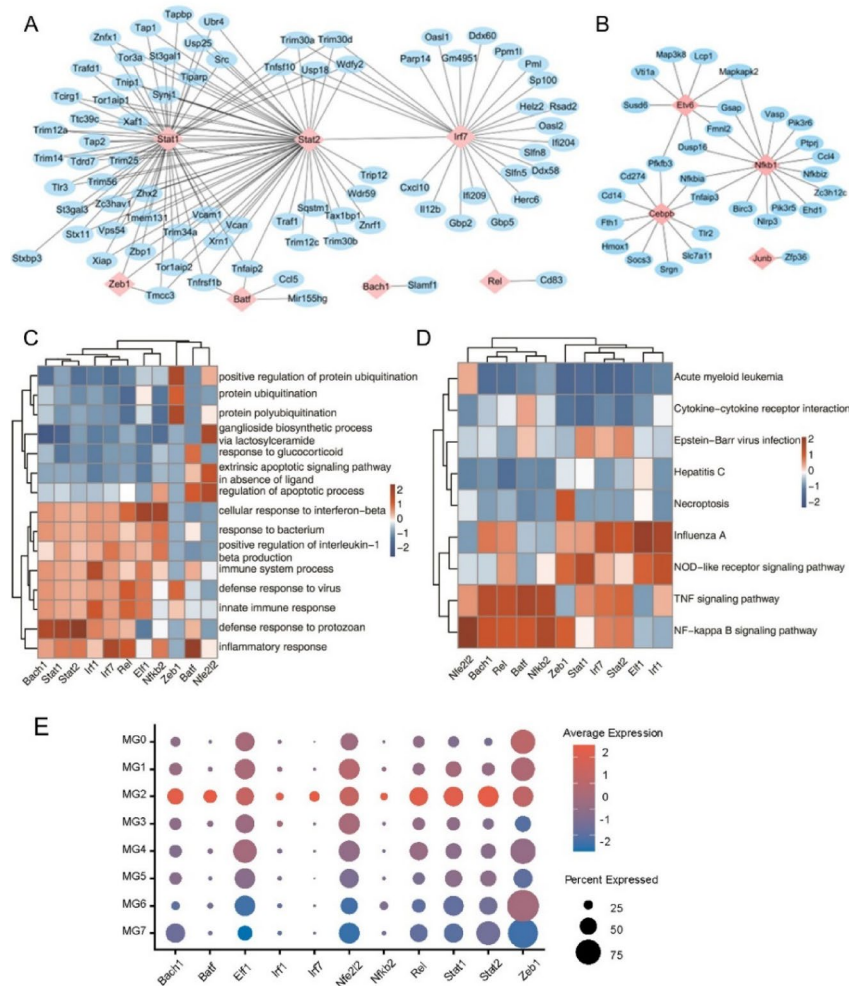
Identification of key transcription factors in microglial inflammatory response after ICH

To further identify the key transcription factors (TFs) involved in regulating neuroinflammation in microglia, we employed SCENIC analysis to construct transcriptional regulatory networks and selected Regulon with score > 20 to display. We mainly focused on the gene clusters associated with inflammation and immune responses, including Cluster 2, Cluster 8 and Cluster 10. The key TFs in microglial inflammatory response after ICH included *Stat2*, *Stat1*, *Irf7*, *Nfkb1*, *Etv6*, *Cebpb*, *Batf*, and *Bach1*. Notably, *Stat2* and *Stat1* were identified as the most central TFs. Notably, Cluster 8 displayed lower regulon scores across its TFs, with *Stat2*, *Stat1*, and *Irf7* regulating the largest number of target genes. As shown in Fig. 5A, *Stat2* and *Stat1* co-regulated a significant number of interferon-stimulated genes(ISGs), including ubiquitin-specific peptidase 18 (*Usp18*) and several from the tripartite motif-containing protein (TRIM) family. USP18 is arguably the ISG with the most important

Fig. 4. The dynamic expression patterns of microglia genes after ICH. (**A**) The bar plot showing the number of differential genes up-regulated and down-regulated in microglia. Red are up-regulated genes and blue are down-regulated genes. (**B**) Analysis of microglial differential genes by TCseq analysis according to their expression patterns during disease progression. (**C**) The bar plot showing the number of microglia's differential genes in TCseq cluster. (**D**) Gene ontology enrichment analysis of biological processes of each TCseq cluster. Top 3 terms were selected for each cluster and heatmap showing the enrichment q-value of these terms (scaled by column).

role in establishing and maintaining long-term desensitization to type I interferon(IFN) signaling[23]. TRIM14, TRIM25, and TRIM30 function downstream of interferon as well as pathogen-recognition receptors, and modulate innate immune responses to bacterial and viral infections by regulating the activation of interferon-regulatory factor 3 (IRF3), IRF7, and NF-κB[24–26]. *Irf7* was found to regulate chemokine genes such as *Cxcl10*, interferon-induced GTP-binding protein genes *Gbp2* and *Gbp5*, and interleukin-12B (*Il12b*). *Irf7* also interacts with *Stat2* and *Stat1*, with a particularly strong interaction with *Stat2*. Enrichment analysis indicated that the target genes regulated by *Stat2*, *Stat1*, and *Irf7* are primarily involved in inflammatory and immune responses, with significant enrichment in the TNF signaling pathway and NOD-like receptor signaling pathway. In Cluster 10, the key TFs included *Nfkb1*, *Etv6*, and *Cebpb*. *Cebpb* encodes the CCAAT Enhancer Binding Protein Beta (C/EBPβ), which upregulates the expression of pro-inflammatory and neurodegeneration-associated genes in microglia[27](Fig. 5B). As depicted in Fig. 5C and E and Fig.S3A, *Stat2*, *Stat1*, and *Irf7* exhibited heightened regulatory activity in microglia across different samples, particularly in the ICH-6 h sample, with the key TFs from Cluster 2 showing predominant expression in the MG2 cluster. Additionally, SCENIC analysis for MG2 cluster, the main inflammation-related microglial subcluster post-ICH, revealed similar result to the combined of Cluster 2, Cluster 8, and Cluster 10 (Fig.S3B). In this study, *Stat2* was found to be the TF with the highest
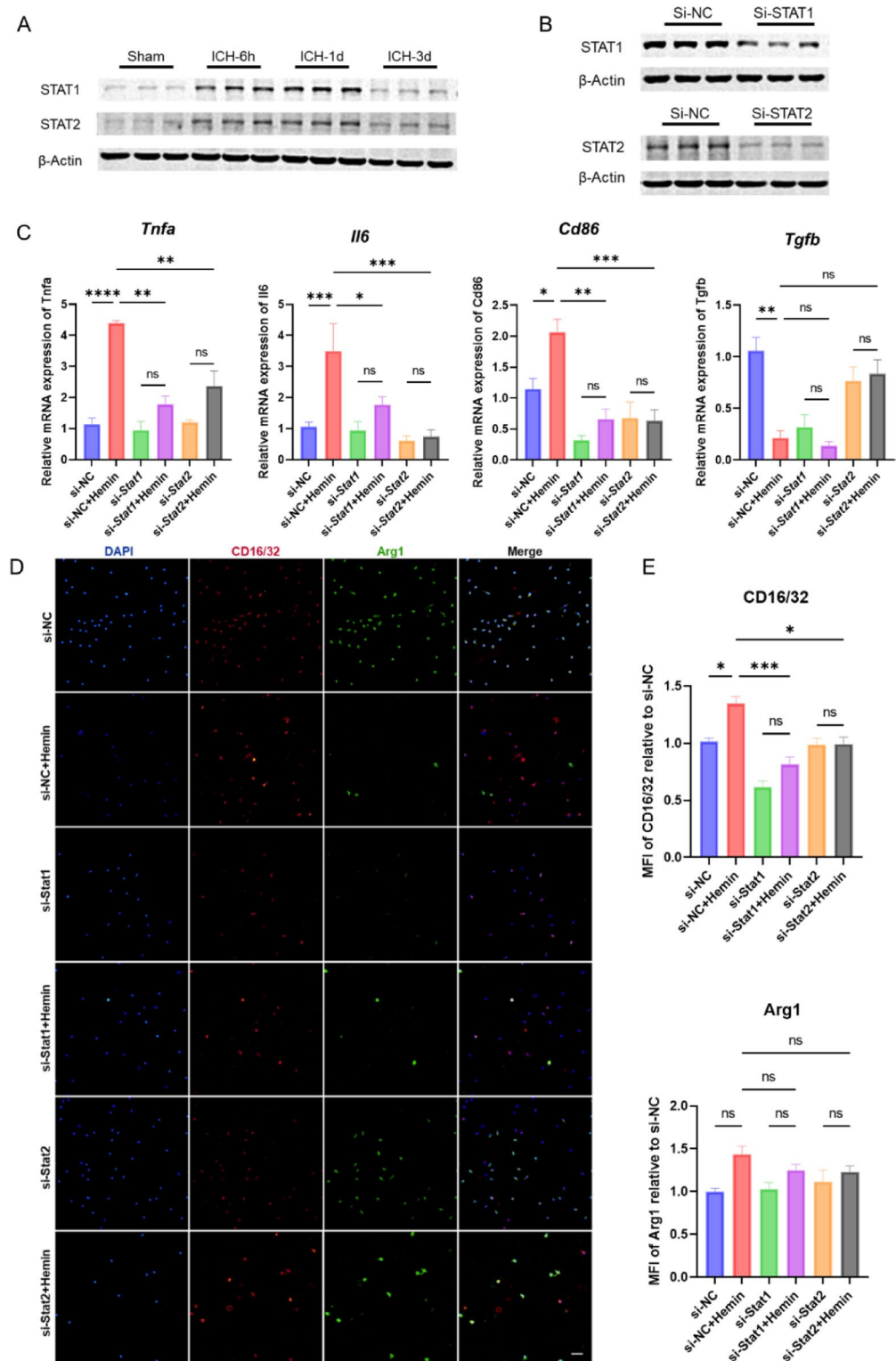
Fig. 5. Identification of key transcription factors in microglial inflammatory response after ICH. Transcriptional regulatory network of microglia gene group Cluster 2 (**A**) and Cluster 10 (**B**). Regulon with score > 20 was selected for visualization, where the red diamond represented transcription factors, the blue oval represented target genes, and the line represented the co-expression association. (**C**). Gene ontology enriched biological processes for key transcription factors in Cluster 2. D. Significantly enriched KEGG pathways for key transcription factors in Cluster 2 (Kanehisa & Goto, 2000). E. Expression of key TFs in microglia subgroups.

transcriptional activity and the largest number of target genes in inflammation-related microglia after ICH, and it mainly co-regulated a large number of target genes with *Stat1*.

Inhibition of *Stat1* and *Stat2* alleviates microglial inflammatory response post-ICH

We validated the role of *Stat2* and *Stat1* in the microglial inflammatory response in both in vivo and in vitro models (Fig.S4A, S4B). In the in vivo model, RT-qPCR and WB demonstrated a significant upregulation of *Stat1* and *Stat2* gene expression in the perihematomal tissue of mice at 6 h and 24 h post-ICH, with expression levels decreasing by 72 h (Fig. 6A, S4C, S4D). For the in vitro model, primary microglial cells were treated with 20 μM Hemin to simulate ICH conditions(Fig.S4B). We utilized siRNA transfection to respectively inhibit the expression of STAT1 and STAT2 (Fig. 6B, S4E, S4F). RT-qPCR results showed that down-regulated STAT1 and STAT2 inhibited the expression of proinflammatory genes *Cd86*, *Tnfa* and *Il6*, but had no significant effect on anti-inflammatory gene *Tgfb* after ICH(Fig. 6C). To further elucidate the role of *Stat1* and *Stat2* in microglial polarization post-ICH, we used relative mean fluorescence intensity (MFI) to evaluate the expression of the traditional M1 marker FcγR III/Ⅱ (CD16/32) and M2 marker arginase1 (Arg1). The immunofluorescence results indicated that the downregulation of STAT1 and STAT2 reduced the expression of CD16/32 in microglia after ICH, but had no significant effect on Arg1 (Fig. 6D and E). Overall, the significant suppression of canonical M1 markers (Cd86, Tnfa, Il6 at mRNA level; CD16/32 at protein level) demonstrates that Stat1/2 knockdown inhibits microglial inflammatory response post-ICH.

Fig. 6. Functional validation of STAT1 and STAT2 in in vitro and in vivo ICH models. (**A**) Western blotting was performed to detect the expression of STAT1 and STAT2 in the perihematoma tissue of ICH mouse model, $n = 3$. (**B**) Primary microglia were transfected with siRNA for 48 h, and the expression of STAT1 and STAT2 was detected by WB, $n = 3$. (**C**) After siRNA transfection inhibited the expression of *Stat1* or *Stat2* in primary microglia, ICH models were constructed in vitro, and the expression levels of *Cd86*, *Tnfa*, *Il6* and *Tgfb* genes were detected by qPCR, $n = 4$. (**D**) CD16/32 and Arg1 immunofluorescence staining of ICH model in vitro after transfection with siRNA, scale $= 50$ μm. (**E**) Relative mean fluorescence intensity (MFI) statistics of CD16/32 and Arg1, $n = 4$, each with at least 3 fields of view. ns, no statistically significance, $*P < 0.05$, $**P < 0.01$, $***P < 0.001$, $****P < 0.0001$. Data are presented as mean ± SEM. A two-sample t-test was employed for comparisons between two groups, while one-way ANOVA was used for comparisons among multiple groups.

Discussion

In this study, we employed snRNA-seq to reveal the cellular heterogeneity following ICH, and to identify the functional changes in specific cell types involved in neural injury and repair. Among the five major cell subpopulations identified in our study, neurons constituted the majority of all detected cells, followed by oligodendrocytes and microglia, and fewer OPCs and astrocytes, which was consistent with the general trend of previous snRNA-seq results in mouse brain tissue[28]. Endothelial cells and smooth muscle cells were not found in cell annotation, which may be due to the small number of cells and low expression level of marker genes. Compared to scRNA-seq, snRNA-seq effectively reduces cell bias and stress responses caused by tissue dissociation, and it is suitable for frozen samples, making it more potential for research on human brain specimens[29]. However, snRNA-seq lacks transcriptome data from the cytoplasm, which, although it reduces background noise in gene detection, also limits the sensitivity for detecting certain genes[30,31]. Thus, integrating snRNA-seq with scRNA-seq and other omics technologies could provide a more comprehensive understanding of cellular heterogeneity in neurological diseases.

Previous studies have demonstrated that following ICH, microglia rapidly undergo activation into the M1 phenotype, with their numbers peaking within 6 h to 1 day. Subsequently, M2 microglia emerge more than 1 day after ICH onset and gradually increase in number, reaching a peak around 14 days. By the time of 21 days post-ICH, both M1 and M2 microglia return to baseline levels[32]. In the pseudotime series analysis, microglia in S5 state exhibited high expression of marker genes for the M2-type microglia (*Arg1* and *Tgfbi*); however, their abundance was limited. This limitation may be attributed to the narrow sampling timeframe employed in this study since neuroprotective microglial subtypes were still present at low levels. To comprehensively investigate phenotypic transformation towards neuroprotective subtypes, it may be necessary to add samples of chronic phase.

We found that *Stat1*, *Stat2* and Irf7 are the primary TFs in inflammation-associated microglia following ICH. Notably, these TFs also exhibited enriched activity in one of the most inflammatory ischemic injury-associated microglial subclusters in another scRNA-seq study of ischemic stroke, which further confirms the significant role of JAK/STAT pathway in neuroinflammation[33]. Type I and III interferon signals activate TYK2 and JAK1, leading to the binding of STAT1 and STAT2 to form heterodimers or homodimers. The STAT1:STAT2 heterodimer combines with interferon regulatory factor 9 (IRF9), constitute the interferon-stimulated gene factor 3 (ISGF3) complex. ISGF3 translocates to the nucleus and binds to interferon-stimulated response elements (ISRE), directly driving the transcription of interferon-stimulated genes (ISGs) that encode key pro-inflammatory cytokines and chemokines(e.g., CXCL10, CCL5). The induced IRF7 further stimulates the expression of type I interferons through a positive feedback loop[34,35]. Additionally, even without IFN stimulation, STAT2 homologous dimers can also bind to IRF9 and ISRE to drive low but persistent ISGs expression[34,36]. Wang et al. demonstrated that curcumin alleviates ICH-induced neuronal apoptosis and neuroinflammation by inhibiting the JAK1/STAT1 pathway[37]. On the other hand, the absence of Stat2 downregulates NF-κB target genes by impairing NF-κB nuclear translocation, thereby suppressing the inflammatory response[38]. These findings collectively suggest that early administration of JAK/STAT pathway inhibitors following ICH may suppress neuroinflammation and mitigate associated neurological damage.

Despite the insights gained into cellular heterogeneity after ICH, this study has several limitations. First, the autologous blood ICH model primarily simulates hematoma compression and the resulting inflammatory response, with minimal microvascular rupture and less severe blood-brain barrier disruption[39,40], which may limit the generalizability of the findings. Second, siRNA transfection may lead to off-target effects or transient inhibition of gene expression, and the functional validation of *Stat1* and *Stat2* was limited to in vitro ICH model, without exploring the detailed mechanisms of their signaling pathway. Future studies should focus on the phosphorylation status of these TFs and their interactions to comprehensively elucidate their roles in the inflammatory response following ICH and other neurological diseases. Additionally, while animal models have been instrumental in this research, applying these findings to humans remains a challenge. Obtaining perihematomal tissue from human ICH cases suitable for single-cell sequencing will be a crucial step in future research.

Conclusion

This study has preliminarily constructed a single-cell transcriptomic atlas of ICH, identified 8 subtypes of microglia after ICH, and uncovering the critical transcription factors involved in the microglial inflammatory response after ICH, particularly *Stat1* and *Stat2*. We believe these findings not only enhance our understanding of cellular heterogeneity and microglial function in ICH but also provide new targets and directions for future research into the mechanisms and treatment of ICH.

Materials and methods
Animals

Adult Male C57BL/6 mice, aged 8–10 weeks and weighing 24–26 g, were purchased from Liaoning Changsheng Biotechnology Co., Ltd. C57BL/6J neonatal mice (within 3 days of birth) were purchased from Shulaibao (Wuhan) Biotechnology Co., Ltd. The mice were housed in a stable and suitable barrier system with controlled temperature and humidity, maintaining a regular 12-hour light/dark cycle with free access to food and water. All experiments conducted in this study were approved by the Ethics Committee of Tongji Hospital, affiliated with Tongji Medical College, Huazhong University of Science and Technology (No.TJH-201909015). Animal care and experimental procedures were strictly conducted following institutional guidelines and complied with the ARRIVE guidelines.

Mouse model of ICH

The model of basal ganglia ICH in mice was established by autologous blood injection. Mice were anesthetized with an intraperitoneal injection of 1% pentobarbital sodium (70 mg/kg; National Pharmaceutical Chemical Reagent Co., Ltd., Shanghai, China), and blood was collected from the retro-orbital venous plexus. 30 µl blood were stereotactic injected into the basal ganglia (AP: +0.5 mm; ML: -2 mm; DV: -3.5 mm) at 1 µl/min. The sham group were injected equal volume of PBS. After 10-minute pause, the needle was withdrawn slowly. Postoperative mice were placed on a thermostatic heating pad until recovery, after which they were returned to the housing environment.

Sample Preparation

Mice were sampled at designated time (sham, 6 h, 24 h, 72 h) after ICH modeling. Mice were euthanized with 1% pentobarbital sodium overdose anesthesia. Brain samples were obtained using brain matrix (1 mm, RWD Life Science, Shenzhen, China). For snRNA-seq, the brain was taken after cardiac perfusion. Deep anesthesia was induced using 1% sodium pentobarbital, and intracardial perfusion was performed with sterile PBS pre-cooled to 4 °C. The brains were rapidly extracted and quickly washed in sterile PBS, blotted dry on absorbent paper, and tissues surrounding the hematoma totaling 3 mm anterior and posterior to the injection site were collected using brain matrix, and the residual intracranial hematoma was removed. Samples were placed in 2 ml cryotubes and rapidly frozen in liquid nitrogen for storage. For snRNA-seq, three mice were prepared per group, resulting in a total of 12 adult mice. All 12 mice were verified to have successful ICH model establishment through behavioral and histological assessments, with no animals excluded due to experimental failure. For sequencing, one sample per group was selected based on comprehensive evaluations of behavioral performance, hematoma size and location, as well as sample quality.

Single-Nucleus RNA sequencing

Sample processing and library construction

Single-nucleus isolation was performed using the Chromium Nuclei Isolation Kit 16 rxns (10x Genomics, Pleasanton, CA, USA) according to the manufacturer's instructions. Then, 9 µl aliquot of the nuclear suspension was mixed with 1 µl of trypan blue, and the concentration of nuclei was determined under a microscope using a hemocytometer, with the count averaged over three replicates. The concentration of the nuclei suspension was adjusted to approximately 1,000 nuclei/µl by adding Wash and Resuspension Buffer. Library construction was carried out using the Chromium Next GEM Single Cell 3′ Reagent Kits v.3.1 (10x Genomics, Pleasanton, CA, USA). After quality control, the libraries were sequenced on the DNBSEQ platform, and FASTQ data were exported for subsequent analysis.

Date processing and quality control

Sequencing data were processed using Cell Ranger (v5.0.1) against the mm10 reference genome and transcriptome (refdata-gex-mm10-2020-A). UMI count matrix was converted into a Seurat object by the R package Seurat (version 4.0.4)[41]. Cells with UMI numbers < 1000, and detected genes < 500 and over 15% mitochondrial-derived UMI counts were considered low-quality cells and removed. Genes detected in less than 5 cells were removed for downstream analyses.

Dimension reduction、unsupervised clustering and Cell-type annotation

After quality control, the UMI count matrix was log normalized. Then top 2000 variable genes were used to create potential Anchors with FindIntegrationAnchors function of Seurat. Subsequently, IntegrateData function was used to integrate data. To reduce the dimensionality of the snRNA-seq dataset, principal component analysis (PCA) was performed on an integrated data matrix. With Elbowplot function of Seurat, top 50 PCs were used to perform the downstream analysis. The main cell clusters were identified with the FindClusters function offered by Seurat, with resolution set as default (res = 0.6). Finally, cells were clustered into 39 major cell types. And then they were visualized with tSNE or UMAP plots. To identify the cell type for each cluster, we detected gene markers for each cell clusters using the "FindMarkers" function in Seurat package (v4.0.4), then we annotated cell types using ScType tools with expanded previously published marker genes of neurons and glial cells[42].

Differential gene expression analysis

Differentially expressed genes (DEGs) were determined with the FindMarkers function from the Seurat package (one-tailed Wilcoxon rank sum test, pvalues adjusted for multiple testing using the Bonferroni correction). For computing DEGs, all genes were probed that the expression difference on a natural log scale was at least 0.5 and the difference of percent of detected cells was at least 0.15 and adjusted pvalue was less than 0.05.

Functional enrichment analysis

Gene Ontology (GO) terms and Kyoto encyclopedia of genes and genomes (KEGG) pathways were identified using KOBAS 2.0[43–45]. Hypergeometric test and Benjamini-Hochberg FDR controlling procedure were used to define the enrichment of each term.

Pseudotime analysis

Monocle2(v2.18.0) was used for pseudotime analysis[46]. DDRTree method with default parameters was used for dimensionality reduction, and branch expression analysis modelling (BEAM) was used to identify specific genes enriched along the evolutionary tracks of each branch. Branch heat maps were created using significant clad-specific genes ($q < 5 \times 10^{-5}$), and various patterns derived from each pseudo-temporal analysis were analyzed by GO.

Time-dependent expression pattern analysis

TCseq packages(https://bioconductor.org/packages/release/bioc/html/TCseq.html)were exploited to identify time-dependent transcriptional alterations in disease progression. First, the average expression level log 2 (TPM/10 + 1) of each gene in each stage among single cells was calculated. Then, the 'timeclust' function was used to cluster different expression patterns.

Transcription factors analysis

From AnimalTFDB website (http://bioinfo.life.hust.edu.cn/AnimalTFDB#! /) obtained 1623 transcription factors (TFs) in mice and 970 TFs target genes, using pySCENIC package (v0.11.2, https://scenic.aertslab.org/) transcription regulation network analysis was carried out on the microglia. TFs were extracted from microglia respectively and co-expression analysis was performed. Co-expression associations of TF and targeted genes were built by the "grn" algorithm from the SCENIC python workflow (version 0.11.2) using default parameters (http://scenic.aertslab.org)[47]. Activated TFs were identified in the AUC matrix. Networks of the modules with TF and their target genes were visualized by Cytoscape (v3.9.1, https://cytoscape.org/).

Cell culture and ICH model in vitro

Primary microglia were isolated using the differential adhesion method. Briefly, mixed glial cell cultures were obtained from the brains of neonatal C57BL/6J mice (within 3 days old) and were initially cultured in poly-D-lysine (PDL)-coated flasks. The cells were maintained in DMEM/F12 medium supplemented with 20% fetal bovine serum (FBS) at 37℃ in a 5% CO2 incubator. After 3 days, the medium was replaced with DMEM/high glucose containing 20% FBS, and the medium was half changed every 3 days. When the astrocytes had reached confluency and a significant number of microglia had adhered to the surface, the microglia were separated and purified with shaking method. Immunofluorescence staining was performed using an Iba-1 antibody to identify the extracted primary microglia, with a cell purity of over 90%.

To establish an in vitro ICH model, primary microglia were treated with hemin (Sigma-Aldrich, St. Louis, MO, USA)[48]. The appropriate concentration of hemin was determined using the Cell Counting Kit-8 (CCK-8). Briefly, primary microglia were seeded at a density of 5000 cells/well in 96-well plates and incubated for 24 h to allow for adherence. Hemin was then added to the medium at various concentrations (0, 5, 10, 20, 30, 40, 50, 70, and 100 µM) and cultured for 24 h. Cell viability was assessed, and the concentration of hemin that resulted in a 50% reduction in cell viability compared to the control group was selected for subsequent experiments to simulate the in vitro ICH microenvironment.

Cell transfection

Primary microglia cultured for 48 h were transfected with siRNAs when the cell density reached 70–90%. Transfection was performed using Lipofectamine 3000 (Thermo Fisher Scientific, Waltham, MA, USA) according to the manufacturer's instructions. Lipofectamine 3000 (3 µL) was diluted in 62.5 µL Opti-MEM (Gibco, Grand Island, NY, USA). Separately, 62.5 µL Opti-MEM was used to dilute the target gene inhibitor or NC inhibitor (3 µL). The two dilutions were then mixed together and incubated at room temperature for 15 min. The resulting mixture was added to each well, bringing the final concentration of the target gene inhibitor or NC inhibitor to 30 nM in a total volume of 869 µL Opti-MEM per well. The cells were then incubated at the incubator. After 48 h of transfection, total RNA was extracted, and the expression levels of the target gene were measured by qPCR to evaluate transfection efficiency. The siRNA used in this study was purchased from RiboBio Co., Ltd. (Guangzhou, China), and the sequences are as follows:

si-*Stat1*: 5'-GCAGCACAACATACGGAAA-3'.
si-*Stat2*: 5'-GGGTGTTACTACCAGGAAA-3'.

Protein extraction and Western blot (WB)

Perihematomal tissues and primary microglial cells were lysed in ice with RIPA buffer solution (Beyotime, Shanghai, China) supplemented with phenylmethylsulfonyl fluoride (PMSF) (1:100, Sigma, St. Louis, MO, USA), phosphatase, and proteinase inhibitors (1:100, both Cell Signaling Technology, Danvers, MA, USA). Protein concentrations were measured by using the BCA Protein Assay Kit (Beyotime, Shanghai, China). Equal quantities of protein (20 µg/lane for tissue and 30 µg/lane for cell) were subjected to 10% SDS-PAGE for electrophoresis separation and then transferred to PVDF membranes. Subsequently, the membranes were incubated with QuickBlock™ Blocking Buffer for Western Blot at room temperature for 15 min to block non-specific binding, and were incubated overnight at 4 ℃ with the primary antibodies STAT1, STAT2 and β-actin (1:1000, Cell Signaling Technology, #14994, #72604 and #4970). Next, the membranes were incubated with Goat Anti-Rabbit IgG-HRP and Goat Anti-Mouse IgG-HRP secondary antibodies (1:10,000; Proteintech Group, #SA00001-2 and #SA00001-1) at room temperature for 1 h. Protein bands were visualized utilizing enhanced chemiluminescence reagents ((ECL Prime Western Blotting Detection Reagent, Beyotime, Shanghai, China) and imaged with ChemiDoc MP system (Bio-Rad, Hercules, CA, USA). Band intensities were semi-quantified utilizing ImageJ software.

Immunofluorescence

Primary microglia were seeded on PDL-coated coverslips in 12-well plates. At the designated experimental time points, the cells were fixed with 4% paraformaldehyde solution for 15–20 min. Permeabilization was carried out using an IF permeabilization solution for 30 min. Non-specific binding was blocked at room temperature using an IF blocking solution for 1 h. The cells were then incubated overnight at 4℃ with the following primary antibodies: Iba1 (1:500, WAKO, #019-19741), CD16/32 (1:100, Thermo Fisher Scientific, #14-0161-82) and

Arg1 (1:100, Abcam, #ab91279). Subsequently, the cells were incubated for 1 h in the dark with the secondary antibodies: Alexa Fluor® 594-conjugated Goat Anti-Mouse IgG (H + L) (1:200, Thermo Fisher, #A-11005) and Alexa Fluor® 488-conjugated Goat Anti-Rabbit IgG (H + L) (1:200, Abcam, #ab150077). Finally, the coverslips were mounted using an anti-fade mounting medium containing DAPI.

RNA extraction and quantitative Real-Time polymerase chain reaction (qPCR) analysis
Total RNA was extracted using RNAiso Plus (Takara, Japan) according to the manufacturer's instruction and quantified with a spectrophotometer. The cDNA was synthesized using PrimeScript™ RT Master Mix (Takara, Japan), and then RT-qPCR was performed using TB Green® Premix Ex Taq™ II (Takara, Japan). The relative expression levels of genes were calculated using the 2-ΔΔCT method with Gapdh as the internal control gene. The primers were synthesized by Tsingke Biological Technology (Beijing, China), and their sequences are as follows:

The forward primer of GAPDH: 5′ GGTTGTCTCCTGCGACTTCA 3′,
The reverse primer of GAPDH: 5′ TGGTCCAGGGTTTCTTACTCC 3′.
The forward primer of *STAT1*: 5′ TCACAGTGGTTCGAGCTTCAG 3′,
The reverse primer of *STAT1*: 5′ CGAGACATCATAGGCAGCGTG 3′.
The forward primer of *STAT2*: 5′ GTTACACCAGGTCTACTCACAGA 3′,
The reverse primer of *STAT2*: 5′ TGGTCTTCAATCCAGGTAGCC 3′.
The forward primer of IL6: 5′ CTGCAAGAGACTTCCATCCAG 3′,
The reverse primer of IL6: 5′ AGTGGTATAGACAGGTCTGTTGG 3′.
The forward primer of TNFA: 5′ CAGGCGGTGCCTATGTCTC 3′,
The reverse primer of TNFA: 5′ CGATCACCCCGAAGTTCAGTAG 3′.
The forward primer of CD86: 5′ GACCGTTGTGTGTGTTCTGG 3′,
The reverse primer of CD86: 5′ GATGAGCAGCATCACAAGGA 3′.
The forward primer of TGFβ: 5′ TGCGCTTGCAGAGATTAAAA 3′,
The reverse primer of TGFβ: 5′ CGTCAAAAGACAGCCACTCA 3′.

Statistical analysis
GraphPad Prism 9 software was used for both data visualization and statistical analysis. Experimental data are presented as mean ± standard error of the mean (SEM). A two-sample t-test was employed for comparisons between two groups, while one-way analysis of variance (ANOVA) was used for comparisons among multiple groups. Statistical significance was defined as $P < 0.05$.

Data availability
The data supporting the findings of this study have been deposited in the Gene Expression Omnibus (GEO) database under accession number [GSE279874]. These data are currently under private status until the publication of this manuscript. Following acceptance and publication of the article, the data will be immediately released to the public, superseding the original embargo date (February 20, 2026). During the peer review process, reviewers can access the data using the following secure token: atsteuqanzajhgb, via the GEO private review link: https://www.ncbi.nlm.nih.gov/geo/query/acc.cgi?acc=GSE279874.

References
1. Sheth, K. N. Spontaneous intracerebral hemorrhage. *N. Engl. J. Med.* **387**, 1589–1596 (2022).
2. Xue, M. & Yong, V. W. Neuroinflammation in intracerebral haemorrhage: immunotherapies with potential for translation. *Lancet. Neurol.* **19**, 1023–1032 (2020).
3. Magid-Bernstein, J. et al. Cerebral hemorrhage: Pathophysiology, Treatment, and future directions. *Circ. Res.* **130**, 1204–1229 (2022).
4. Lim-Hing, K. & Rincon, F. Secondary hematoma expansion and perihemorrhagic edema after intracerebral hemorrhage: from bench work to practical aspects. *Front. Neurol.* **8**, 74 (2017).
5. Zhang, P. et al. Single-Cell RNA sequencing reveals the evolution of the immune landscape during perihematomal edema progression after intracerebral hemorrhage. *J. Neuroinflamm..* **21**, 140 (2024).
6. Xiang, R. et al. Spatiotemporal transcriptomic maps of mouse intracerebral hemorrhage at Single-Cell resolution. *Neuron* **113**, 2102–2122 (2025).
7. Zhao, X. et al. Transcription factor Nrf2 protects the brain from damage produced by intracerebral hemorrhage. *Stroke* **38**, 3280–3286 (2007).
8. Zeng, J. et al. Isoliquiritigenin alleviates early brain injury after experimental intracerebral hemorrhage via suppressing ROS- And/Or NF-Kappab-Mediated NLRP3 inflammasome activation by promoting Nrf2 antioxidant pathway. *J. Neuroinflamm..* **14**, 119 (2017).
9. Palahati, A. et al. TonEBP: A key transcription factor in microglia following intracerebral hemorrhage Induced-Neuroinflammation. *Int. J. Mol. Sci.* **25**, (2024).
10. Wang, L. et al. Microglial Lcn2 knockout enhances chronic intracerebral hemorrhage recovery by restoring Myelin and reducing inflammation. *Theranostics* **15**, 4763–4784 (2025).
11. Hu, D. et al. NR4a2 attenuates early brain injury after intracerebral hemorrhage by promoting M2 microglial polarization via TLR4/TRAF6/NF-Kappab pathway Inhibition. *Cell. Mol. Life Sci.* **82**, 262 (2025).
12. Xu, Y. et al. Peripheral cytokine Interleukin-10 alleviates perihematomal edema after intracerebral hemorrhage via Interleukin-10 Receptor/JAK1/STAT3 signaling. *CNS Neurosci. Ther.* **30**, e14796 (2024).
13. Konishi, H. et al. Siglec-H is a microglia-Specific marker that discriminates microglia from CNS-Associated macrophages and CNS-Infiltrating monocytes. *Glia* **65**, 1927–1943 (2017).

14. Khalaf, G. et al. Mutation of Proteolipid Protein 1 Gene: From Severe Hypomyelinating Leukodystrophy to Inherited Spastic Paraplegia. *Biomedicines*. 10, (2022).
15. Paolicelli, R. C. et al. Microglia States and nomenclature: A field at its crossroads. *Neuron* 110, 3458–3483 (2022).
16. Qi, X. et al. Long Non-Coding RNA SNHG14 promotes microglia activation by regulating Mir-145-5P/PLA2G4a in cerebral infarction. *Neuroscience* 348, 98–106 (2017).
17. Popiolek-Barczyk, K. et al. The CCL2/CCL7/CCL12/CCR2 pathway is substantially and persistently upregulated in mice after traumatic brain Injury, and CCL2 modulates the complement system in microglia. *Mol. Cell. Probes*. 54, 101671 (2020).
18. Colonna, M. & Brioschi, S. Neuroinflammation and neurodegeneration in human brain at Single-Cell resolution. *Nat. Rev. Immunol.* 20, 81–82 (2020).
19. Li, D., Chen, M., Meng, T. & Fei, J. Hippocampal microglial activation triggers a Neurotoxic-Specific astrocyte response and mediates Etomidate-Induced Long-Term synaptic Inhibition. *J. Neuroinflamm.*. 17, 109 (2020).
20. Ji, J. et al. Antagonizing peroxisome Proliferator-Activated receptor gamma facilitates M1-to-M2 shift of microglia by enhancing autophagy via the LKB1-AMPK signaling pathway. *Aging Cell*. 17, e12774 (2018).
21. Hammond, T. R. et al. Single-Cell RNA sequencing of microglia throughout the mouse lifespan and in the injured brain reveals complex Cell-State changes. *Immunity* 50, 253–271 (2019).
22. Kent, S. A. & Miron, V. E. Microglia regulation of central nervous system Myelin health and regeneration. *Nat. Rev. Immunol.* 24, 49–63 (2024).
23. Schneider, W. M., Chevillotte, M. D. & Rice, C. M. Interferon-Stimulated genes: A complex web of host defenses. *Annu. Rev. Immunol.* 32, 513–545 (2014).
24. Ozato, K., Shin, D., Chang, T. & Morse, H. C. R. TRIM family proteins and their emerging roles in innate immunity. *Nat. Rev. Immunol.* 8, 849–860 (2008).
25. Li, X. et al. Emerging discoveries on the role of TRIM14: from diseases to immune regulation. *Cell. Death Discov*. 10, 513 (2024).
26. Yang, L. & Xia, H. TRIM proteins in inflammation: from expression to emerging regulatory mechanisms. *Inflammation* 44, 811–820 (2021).
27. Ndoja, A. et al. Ubiquitin ligase COP1 suppresses neuroinflammation by degrading C/EBPbeta in microglia. *Cell* 182, 1156–1169 (2020).
28. Morabito, S. et al. Single-Nucleus chromatin accessibility and transcriptomic characterization of alzheimer's disease. *Nat. Genet.* 53, 1143–1155 (2021).
29. Denisenko, E. et al. Systematic assessment of tissue dissociation and storage biases in Single-Cell and Single-Nucleus RNA-Seq workflows. *Genome Biol*. 21, 130 (2020).
30. Wu, H., Kirita, Y., Donnelly, E. L. & Humphreys, B. D. Advantages of Single-Nucleus over Single-Cell RNA sequencing of adult kidney: rare cell types and novel cell States revealed in fibrosis. *J. Am. Soc. Nephrol*. 30, 23–32 (2019).
31. Koenitzer, J. R., Wu, H., Atkinson, J. J., Brody, S. L. & Humphreys, B. D. Single-Nucleus RNA-Sequencing profiling of mouse Lung. Reduced dissociation bias and improved rare Cell-Type detection compared with Single-Cell RNA sequencing. *Am. J. Respir Cell. Mol. Biol*. 63, 739–747 (2020).
32. Tschoe, C., Bushnell, C. D., Duncan, P. W., Alexander-Miller, M. A. & Wolfe, S. Q. Neuroinflammation after intracerebral hemorrhage and potential therapeutic targets. *J. Stroke*. 22, 29–46 (2020).
33. Zheng, K. et al. Single-Cell RNA-Seq reveals the transcriptional landscape in ischemic stroke. *J. Cereb. Blood Flow. Metab.* 42, 56–73 (2022).
34. Blaszczyk, K. et al. The unique role of STAT2 in constitutive and IFN-Induced transcription and antiviral responses. *Cytokine Growth Factor. Rev.* 29, 71–81 (2016).
35. Philips, R. L. et al. The JAK-STAT pathway at 30: much Learned, much more to do. *Cell* 185, 3857–3876 (2022).
36. Duodu, P., Sosa, G., Canar, J., Chhugani, O. & Gamero, A. M. Exposing the two contrasting faces of STAT2 in inflammation. *J. Interferon Cytokine Res.* 42, 467–481 (2022).
37. Wang, F. et al. Curcumin attenuates intracerebral Hemorrhage-Induced neuronal apoptosis and neuroinflammation by suppressing JAK1/STAT1 pathway. *Biochem. Cell. Biol.* 100, 236–245 (2022).
38. Alazawi, W. et al. Stat2 loss leads to Cytokine-Independent, Cell-Mediated lethality in LPS-Induced sepsis. *Proc. Natl. Acad. Sci. U S A*. 110, 8656–8661 (2013).
39. Jia, P. et al. Profiling of blood-Brain barrier disruption in mouse intracerebral hemorrhage models: collagenase injection Vs. Autologous arterial whole blood infusion. *Front. Cell. Neurosci*. 15, 699736 (2021).
40. Fang, J., Song, F., Chang, C. & Yao, M. Intracerebral hemorrhage models and behavioral tests in rodents. *Neuroscience* 513, 1–13 (2023).
41. Butler, A., Hoffman, P., Smibert, P., Papalexi, E. & Satija, R. Integrating Single-Cell transcriptomic data across different Conditions, Technologies, and species. *Nat. Biotechnol*. 36, 411–420 (2018).
42. Ianevski, A., Giri, A. K. & Aittokallio, T. Fully-Automated and Ultra-Fast Cell-Type identification using specific marker combinations from Single-Cell transcriptomic data. *Nat. Commun.* 13, 1246 (2022).
43. Kanehisa, M. & Goto, S. K. E. G. G. Kyoto encyclopedia of genes and genomes. *Nucleic Acids Res*. 28, 27–30 (2000).
44. Kanehisa, M., Furumichi, M., Sato, Y., Matsuura, Y. & Ishiguro-Watanabe, M. KEGG: biological systems database as a model of the real world. *Nucleic Acids Res*. 53, D672–D677 (2025).
45. Xie, C. et al. KOBAS 2.0: A web server for annotation and identification of enriched pathways and diseases. *Nucleic Acids Res*. 39, W316–W322 (2011).
46. Qiu, X. et al. Single-Cell MRNA quantification and differential analysis with census. *Nat. Methods*. 14, 309–315 (2017).
47. Hentze, M. W., Castello, A., Schwarzl, T. & Preiss, T. A brave new world of RNA-Binding proteins. *Nat. Rev. Mol. Cell. Biol.* 19, 327–341 (2018).
48. Shi, Y. et al. Salvianolic acid a inhibits ferroptosis and protects against intracerebral hemorrhage. *Sci. Rep.* 14, 12427 (2024).

Author contributions

Funding

Declarations

Competing interests
The authors declare no competing interests.

Additional information
Supplementary Information The online version contains supplementary material available at https://doi.org/10.1038/s41598-025-24675-4.

Correspondence and requests for materials should be addressed to C.P. or Z.T.

Reprints and permissions information is available at www.nature.com/reprints.

Publisher's note Springer Nature remains neutral with regard to jurisdictional claims in published maps and institutional affiliations.